Correlation Measurements for Carbon Nanotubes with Quantum Defects

Min-Ken Li,* Simone Dehm, Manfred M. Kappes, Frank Hennrich, and Ralph Krupke*

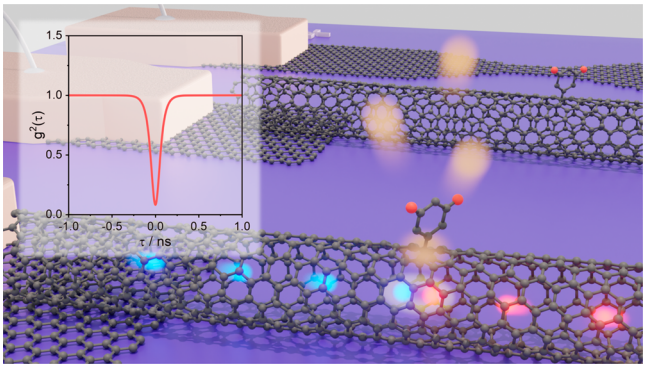

ABSTRACT: Single-photon sources are essential building blocks for the development of photonic quantum technology. Regarding potential practical application, an on-demand electrically driven quantum-light emitter on a chip is notably crucial for photonic integrated circuits. Here, we propose functionalized single-walled carbon nanotube field-effect transistors as a promising solid-state quantum-light source by demonstrating photon antibunching behavior via electrical excitation. The sp^3 quantum defects were formed on the surface of (7, 5) carbon nanotubes by 3,5-dichlorophenyl functionalization, and individual carbon nanotubes were wired to graphene electrode pairs. Filtered electroluminescent defect-state emission at 77 K was coupled into a Hanbury Brown and Twiss experiment setup, and single-photon emission was observed by performing second-order correlation function measurements. We discuss the dependence of the intensity correlation measurement on electrical power and emission wavelength, highlighting the challenges of performing such measurements while simultaneously analyzing acquired data. Our results indicate a route toward room-temperature electrically triggered single-photon emission.

KEYWORDS: *carbon nanotubes, graphene, defects, excitons, electroluminescence, second-order correlation function measurement*

INTRODUCTION

With the increased demand for data transmission and information processing, technology based on optics has played an increasingly important role. For instance, since the demonstration of optical fibers as a technologically feasible platform for telecommunication, optical networks have replaced a large proportion of electrical communication media.[1] The emergence of photonics integrated circuits has also led to the realization of multifunctional devices by combining individual photonic components on a chip.[2] However, the challenges of developing suitable on-demand light sources that are at the same time compatible with on-chip integration hinder the progress. Meanwhile, in the context of quantum technologies, photons have been demonstrated as a system for quantum information processing protocols[3,4] owing to their high-speed transmission and low-noise nature.[5] Despite the rapid advancement of electrically driven quantum-light sources in various material systems including quantum dots,[6,7] atomic defects in diamond,[8,9] and 2D materials,[10,11] the deployment of solid-state quantum emitters on chips with compatibility for hybrid systems and potential scalability remains elusive as yet.

Single-walled carbon nanotubes (SWCNTs) are among the most promising systems for realizing on-chip quantum emitters.[12,13] Their versatile light emission in the near-infrared, including the telecom band depending on the chiral index[14] and excitation modes,[15,16] facilitates the integration with optical fiber communication. Besides, compatibility with various photonics platforms[17,18] has been studied, and demonstrations of overcoming scalability challenges have also been reported.[19−21] Indeed, SWCNTs as quantum-light sources have been demonstrated via both optical[22] and electrical[23] excitation. However, their lack of exciton localization sites, the essence of nonclassical light emission, unless at very low temperatures,[23] makes practical implementation unrealistic. This demand can be addressed by forming sp^3 quantum defects (0D) at the sidewall of SWCNTs through mild oxidation[24,25] or covalent alkyl- and aryl-functionalization.[26−28] These sp^3 defects can serve as exciton traps with potential depths of 100−300 meV, which provide alternative pathways for exciton radiative recombina-

tion,[29,30] resulting in superior emission yields (from <1% up to 28%)[31] and extending the single-photon emission range of SWCNTs up to room temperature.[32,33] However, the advantages of correspondingly functionalized SWCNTs in the development of on-chip quantum photonics as aforementioned have not yet been fully explored. A few works have studied electrically triggered light emission of carbon nanotubes with sp^3 quantum defects,[34−36] which would be the first step toward on-chip quantum emitters. To the best of our knowledge, functionalized carbon nanotubes as nonclassical emitters have so far only been demonstrated in the context of optical excitation.

In this work, we demonstrate electrically driven single-photon emission at 77 K from defect-state electroluminescent emission of (7, 5) carbon nanotube field-effect transistors functionalized by introducing aryl sp^3 quantum defects with aryl diazonium salts. The second-order correlation function measurement was carried out based on the Hanbury Brown and Twiss experiment with the functionalized carbon nanotube emitters cooled down by liquid nitrogen in an optical cryostat. We also compare the recorded coincidence histograms as a function of the applied electrical power or emission wavelength including data from our previous study regarding electrically triggered nonclassical emission of pristine carbon nanotubes below 4 K.[23] Finally, we discuss and demonstrate how to improve experiment and device performance, for instance, via passivation, to further progress in developing an on-demand electrically driven room-temperature single-photon source.

RESULTS AND DISCUSSION

To study single-photon emission, we used functionalized (7, 5) carbon nanotubes and integrated them into field-effect transistors with CVD graphene electrodes in this work. The pristine (7, 5) semiconducting single-walled carbon nanotube (sc-SWCNT) suspension was prepared from CoMoCAT by polyfluorene (PFO) p olymer-wrapping i n t oluene.[37] Gel filtration c hromatography w as f ollowed f or p urification and length sorting. The pristine (7, 5) SWCNT suspension has an average length of around 550 nm, as shown in the length distribution in Figure S1, and has a high (7, 5) chirality enrichment, which can be seen in the photoluminescence excitation map (PLE) in Figure 1a. The E_{11} optical transition (1050 nm) of (7, 5) carbon nanotubes appeared in the PLE map while exciting the suspension at the E_{22} optical transition (657 nm). Weak emission sidebands associated with RBM and K-momentum dark exciton phonon sidebands[38−41] can also be noticed but no visible emission from sidewall defects nor other carbon nanotube chiralities.[24,25,42] The pristine suspension was further functionalized by adding reactive dichlorobenzene dopants to create 3,5-dichlorophenyl-functionalized sp^3 quantum defects as we reported in a recent work.[36] PLE measurement (Figure 1b) was performed on the as-prepared functionalized suspension to confirm the sp^3 defect formation in which the red-shifted defect-induced emission bands, denoted here as E_{11}^* and E_{11}^{*-}, can be observed.[31] The defect-state emission band originates from the localization of excitons at deep traps (on the order of hundreds meV) and spreads over a rather wide wavelength range mainly due to the diverse binding configurations o f t he a ryl g roup t o t he c arbon nanotube lattice.[43−46]

The functionalized (7, 5) SWCNTs were integrated into three-terminal field-effect transistors via DC dielectrophoresis[47] in which monolayer CVD graphene acted as the source-drain electrode pairs with 150−200 nm gap size and the heavily p-doped Si as the back-gate; see the Methods Section and Figure S2. Dielectrophoretic deposition conditions were adjusted to obtain devices with single or few tubes, and a representative SEM image of a carbon nanotube/graphene device is shown in Figure 4b. Devices were electrically wire bonded and mounted into the optical cryostat of our near-infrared optical microscopy and spectroscopy setup. The cryostat was fixed on a motorized *xy* scanning stage to allow precise positioning of the emitter. This is especially crucial when coupling emitted light into the single-mode optical fiber to perform second-order correlation function measurements. More details will be discussed later. The device was vacuum annealed after the cryostat had been evacuated below 10^{-6} mbar and subsequently cooled to 77 K without breaking the vacuum. Transconductance characteristics, examples displayed in Figure S11a,b, and electroluminescence measurements were carried out before moving on to second-order correlation function measurements. The constant source-drain current mode was implemented to reliably drive devices for electroluminescence,[36] and the emitted light was analyzed by a linear InGaAs photodiode array with a spectral response range between 950 to 1610 nm. All spectra were calibrated by the relative spectral sensitivity of the setup.[48]

Additional setup alignment was necessary to switch from electroluminescence measurement to intensity correlation measurement; see the Methods Section, where the emission light needs to be guided into a fiber-based 50/50 beam splitter for a Hanbury Brown and Twiss (HBT) experiment as shown in Figure 1c. The reason lies in the fact that the *xy* lateral focus position to couple light into the single-mode fiber via a reflective collimator is different from dispersing light onto the InGaAs photodiode for the electroluminescence measurement. The focus position precision for the collimator coupling was also more demanding. To accommodate the issue, during the device fabrication process, we patterned one extra graphene field-effect transistor in a bowtie structure that can act as a bright and stable incandescent light emitter[49] for light-coupling alignment; see Figure S3. As we know the relative positions between the graphene strip and other SWCNT devices, once we finished the alignment, we could simply shift from the graphene strip to any specific SWCNT device by controlling the motorized positioning stage. The setup schematic in Figure 1c points out the important components required for the second-order correlation function measurement, including the motorized stage and the reflective collimator behind the objective for positioning and light collection, a 50/50 fused fiber coupler, and two single-photon detectors with the time arrival analyzer in compliance with the Hanbury Brown and Twiss experiment, and spectral filters.[33,50] As will be discussed in detail in the later part, spectral filtering is still important owing to the emission stability over a long data acquisition time and the potential existence of multiple emission spots (e.g., more than one quantum defect). An example coincidence histogram of intensity correlation measurement at 77 K without inserting a spectral filter is shown in Figure S4. Despite being able to acquire electroluminescence spectra with narrow line width and high spectral purity, the possibility of having two (or more) identical quantum defects and additional emission related to mobile excitons cannot be completely ruled out and leads to a reduced single-photon purity. The single-photon purity refers to the probability of emitting a single photon instead of multiple photons, which can be quantified by the value of the second-order correlation function at zero-time delay, $g^2(0)$. Thoughts on improving the

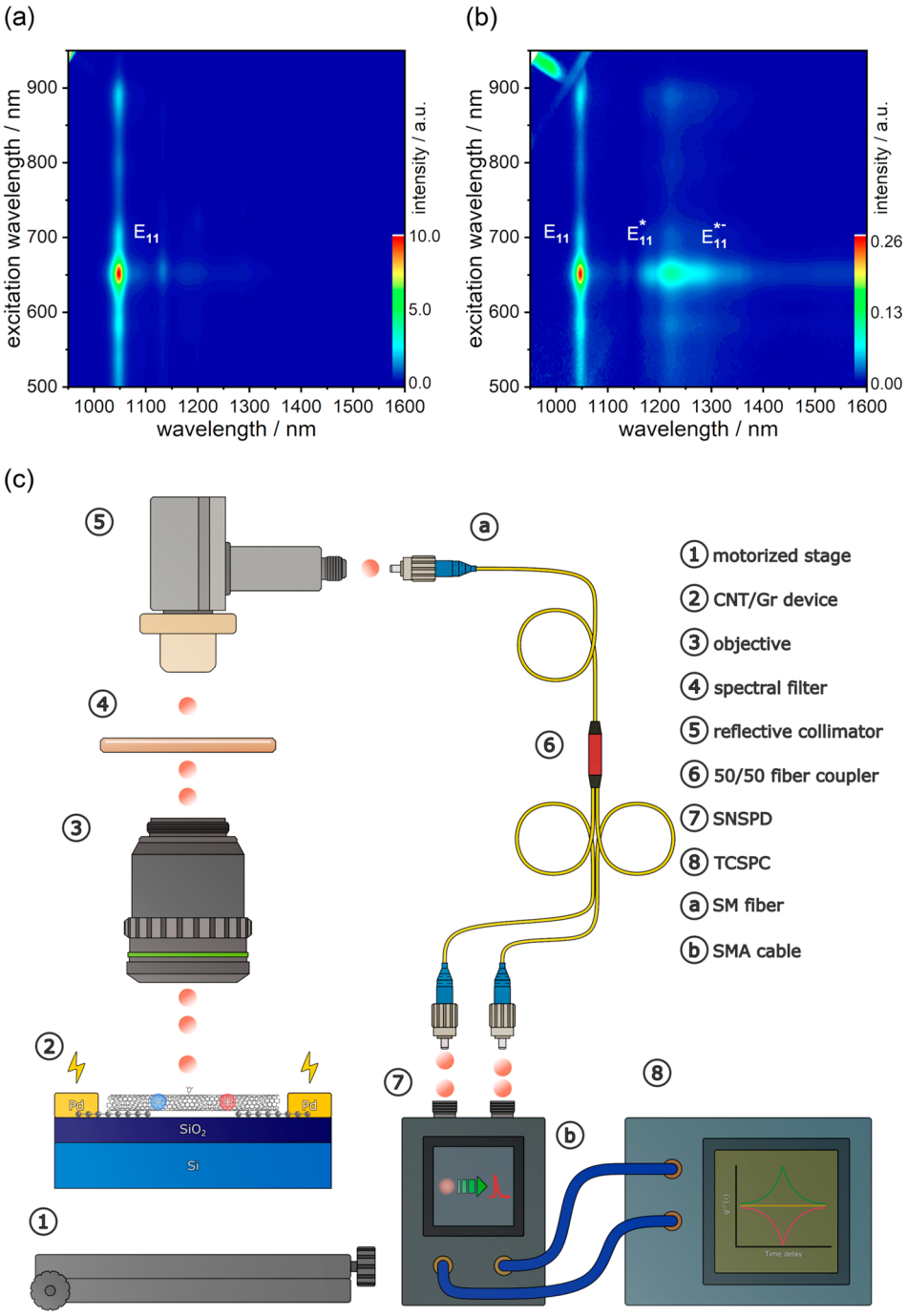

Figure 1. Photoluminescence excitation map of the suspension from polymer-wrapped (7, 5) carbon nanotubes dispersed in toluene (a) before introducing sp^3 sidewall defects with 3,5-dichlorobenzene functionalization and (b) after the functionalization process. E_{11} optical transition and the red-shifted defect-state emission (E_{11}^* and E_{11}^{*-}) are labeled. (c) Experiment setup schematics for the intensity correlation measurement of electrically driven light emission from functionalized carbon nanotubes based on the Hanbury Brown and Twiss configuration. The emitted photons were coupled into a single-mode 50/50 fused fiber coupler via a reflective collimator and used to trigger two independent superconducting single-photon detectors (SSPDs). Photon statistics were recorded by using time-correlated single-photon counting (TCSPC) in the histogram or time-tagged time-resolved (TTTR) mode. Each of the crucial components in the setup is noted in the figure.

results by moving toward measurements without the need for spectral filters or cryogenic temperature are discussed at the end.

The coincidence histograms in which antibunching behaviors were observed at 77 K and the electroluminescence spectra measured before starting the second-order correlation measurements are shown in Figure 2. The best single-photon purity recorded in this work, around 92%, was observed from the functionalized (7, 5) SWCNT device by filtering the excitonic defect-state emission with the lowest transition energy (E_{11}^{*-}) via a 1300 nm bandpass filter, as shown in Figure 2a,b. In the case of Figure 2c,d, a 1350 nm long-pass filter was inserted to transmit only the trionic defect-state emission (E^*_T)[36,51] and resulted in antibunching with around 74% single-photon purity in the intensity correlation measurement. The data with the lowest single-photon purity are shown in Figure 2e,f with a value of around 60%. For this measurement, a 1200 nm bandpass filter

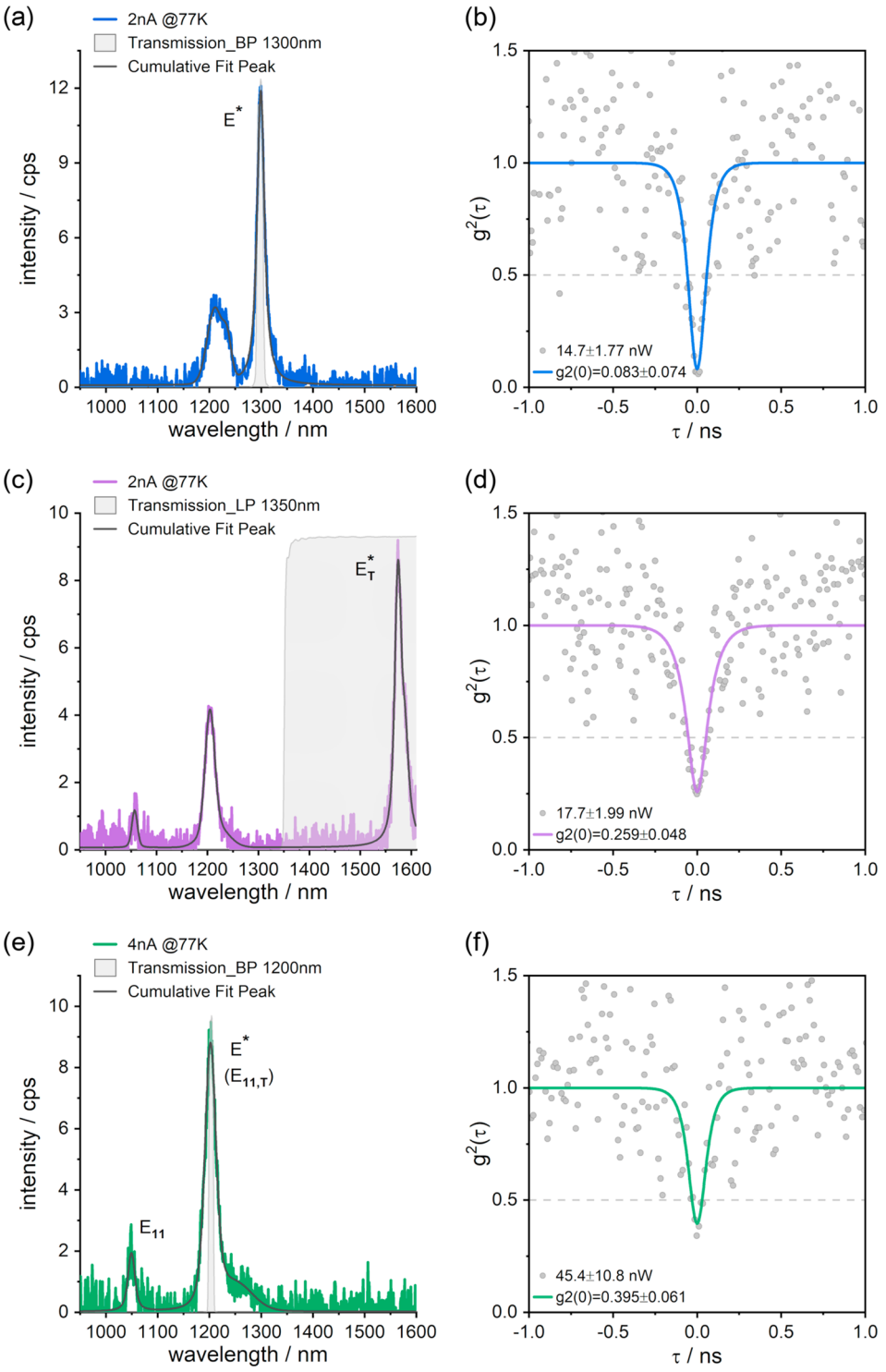

Figure 2. (a), (c), (e) Electroluminescence (EL) spectra of three different functionalized (7, 5) devices measured at 77 K under constant source-drain current excitation of 2, 2, and 4 nA, respectively, as indicated in the figures. The gate voltages were kept at 0 V for all three correlation measurements. The intrinsic excitonic, E_{11} (trionic, $E_{11,T}$), emission, as well as the excitonic and trionic defect-state emissions, E* and E^*_T, are marked. EL spectra were fitted with Voigt functions and were overlapped with the transmission spectra (gray area) of respective spectral filters indicating the filtered light emission for the intensity correlation measurement at 77 K. (b), (d), (f) The respective coincidence histograms measured at 77 K by collecting spectrally filtered electroluminescence. The histograms were accumulated with 8 ps time resolution for (b), (d), and 12 ps for (f) using TCSPC software for data acquisition and analysis. Fitting curves are presented showing antibunching behavior with the second-order correlation function at zero-time delay $g^2(0)$ equaling 0.08, 0.26, and 0.40, respectively. The dashed gray lines served as a guide for the eye for $g^2(0) = 0.5$.

was used for spectral filtering. Apart from the uncertainty that more than one emission center could be active, the similarity in terms of emission position of the excitonic defect-state emission (E_{11}*) and the trionic emission ($E_{11,T}$) could also explain a

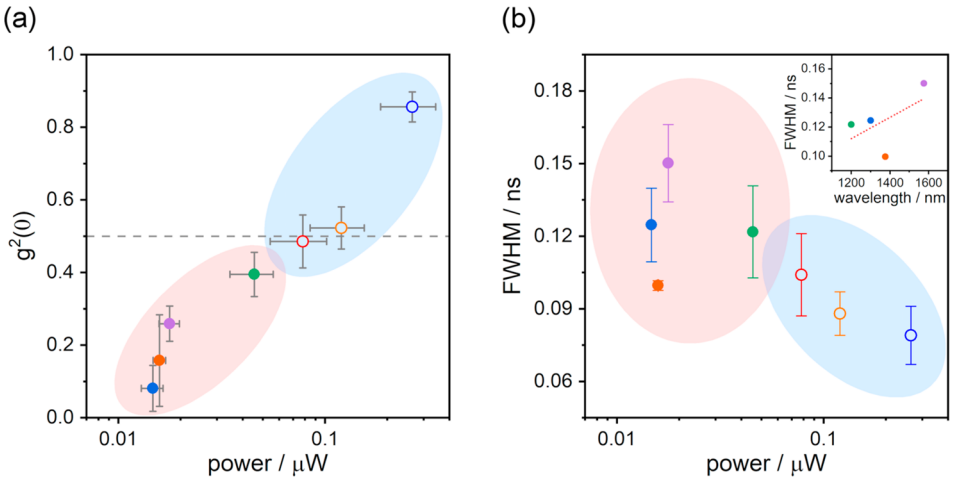

Figure 3. (a) Second-order correlation function at zero-time delay extracted from the fitted values versus the applied electrical power. The solid circles correspond to the intensity correlation measurement of functionalized (7, 5) SWCNTs at 77 K (red area), and the open circles are data adapted from ref 23 measured at 1.6 K for pristine (9, 7) SWCNTs (blue area). The color of the solid circles refers to the results shown in Figure 2 and Figure S9. The *y* error bars stand for the standard deviation derived from the photon antibunching fit. The *x* error bars indicate the standard deviation of the recorded electrical power. (b) Full-width at half-maximum (fwhm) acquired from the fit results versus the electrical power. The inset represents the wavelength dependence of the extracted fwhm values.

limited purity. In our recent work, we already pointed out the difficulty of distinguishing between the defect-state emission and the intrinsic trionic emission.[36] All histogram curves were fitted by the sum of two exponential functions $g^2(\tau) = 1 - c_1 e^{-\gamma_1|\tau-\tau_0|} - c_2 e^{-\gamma_2|\tau-\tau_0|}$, where $c_1 < 0$ and $c_2 > 0$ indicate the amplitudes of bunching and antibunching, γ_1 and γ_2 represent the decay rates, and τ_0 corresponds to the zero-time delay of the antibunching dip, adapted from our previous work.[23] The values of the source-drain current bias for electrical excitation, average electrical power, and second-order correlation function at zero-time delay were extracted from fits and are provided in Figure 2.

The extracted values of the antibunching dip at the zero-time delay, $g^2(0)$, from the intensity correlation measurement are shown in Figure 3a as a function of applied electrical power. Data adapted from our previous work of waveguide-integrated nonclassical light emitter from pristine (9, 7) carbon nanotubes below 4 K[23] are included for comparison purposes. At first glance, there seems to be a linear relation between the electrical power and the $g^2(0)$ value disregarding the presence of sp^3 quantum defects. However, one needs to note that the data were acquired at different temperatures, marked with red for 77 K and blue for 1.6 K separately. It has been pointed out in the literature that the probability of nonclassical emission due to exciton localization in an unstable electrostatic environment greatly depends on the temperature.[52] An in-depth study of the electrical power dependence of the antibunching from the functionalized carbon nanotubes was not the main focus of this work; nevertheless, a general picture was that the lower the electrical power, the better is the $g^2(0)$ value, leading to a higher probability of single-photon emission. Part of the explanation may relate to one of the general challenges for electrically driven quantum emitters, namely, how to concentrate the radiative recombination of electron−hole pairs at the defects instead of surroundings.[53] Also electrical power-dependent spectral purity of defect-state emission plays a role, which could be affected also by the defect density or characteristic displacement between defects. Unfortunately, to the best of our knowledge, a comprehensive study of spectral evolution as a function of triggering power or defect number/density at single (few) nanotube levels is still missing. Figure 3b presents the full-width at half-maximum (fwhm) of the antibunching curves as a function of electrical power, which correlates with the emission lifetime of (functionalized) SWCNTs.[29] Comparison of functionalized and pristine SWCNTs would not be conclusive as the measurement conditions were quite different. However, a trend between fwhm and the emission wavelength could be observed (see Figure 3b inset), which is roughly in agreement with the sp^3 defect trap depths.[29,30] Throughout the course of this work, we recorded 25 coincidence histograms in which 11 show different degrees of photon antibunching, and 4 of them exhibit $g^2(0)$ values below 0.5 with spectral filtering.

For the coincidence histograms displayed in Figure 2, we used the time-tagged time-resolved mode of time-correlated single-photon counting (TCSPC) software to compile coincidence histograms out of the continuous stream of electric pulses generated by the two superconducting single-photon detectors. The signal-to-noise ratio is enhanced when using bidirectional start−stop events to compose the histograms. However, for this method, the system time delay, due for instance to fiber/cable and electronics delay, has to be taken into account and is critical to compensate for the time offset, as demonstrated in Figure S5. To determine the constant time offset of our system, we replaced the SWCNT device with a 1550 nm laser diode and generated a photon bunching signal by operating the laser diode in the subthreshold regime, as described in the work of Tan et al.;[54] see the Methods Section. In general, the bunching peak recorded, shown in Figure S6, had an amplitude lower than that reported. Aside from the difference in emission wavelength, since our laser diode ran without distributed feedback to suppress the side modes, and therefore mode partitioning,[55] this may disturb the photon bunching outcome.

Simultaneous to the time tagging of the incoming photons, we continuously measured the voltage that was applied by the source-measurement unit to maintain the constant current bias. Figure 4a shows such a trace of the power, which varies substantially over time. The data are the trace that corresponds to the coincidence histogram shown in Figure 2d, but it is representative of what we have observed. For the other

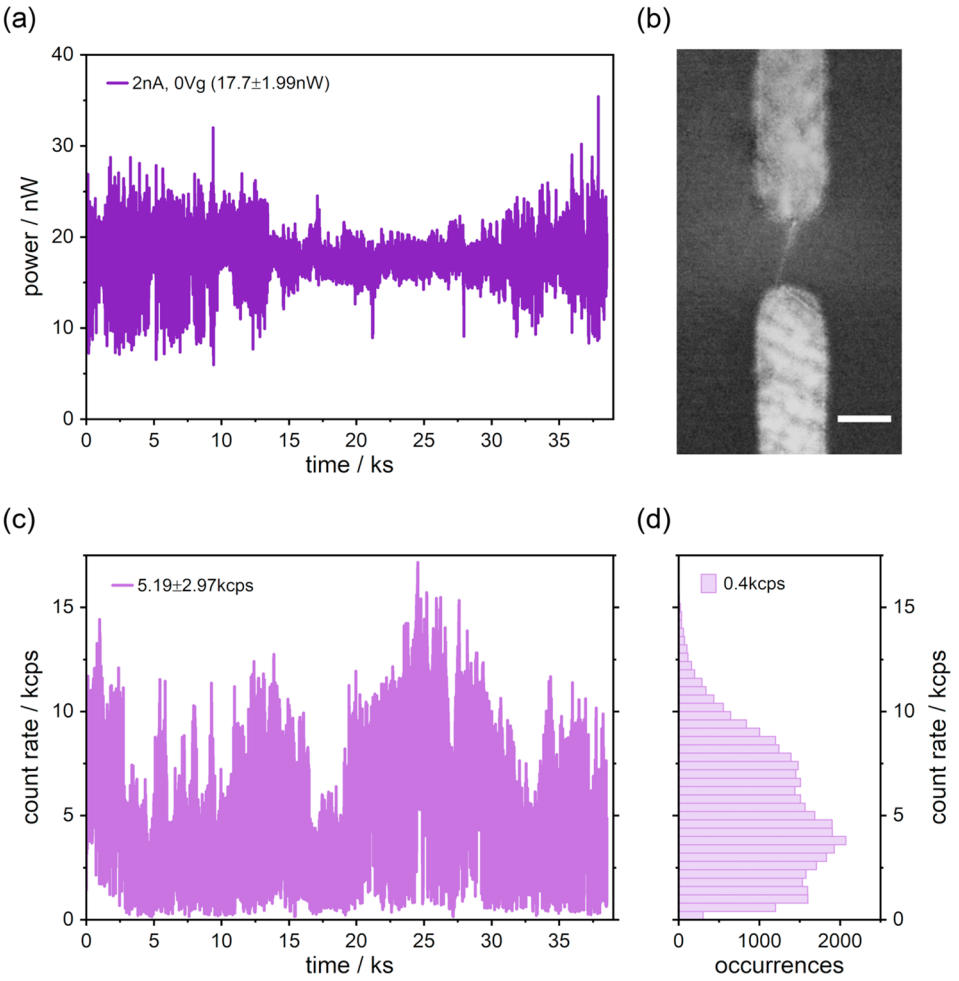

Figure 4. (a) Time trace of the applied electrical power for the intensity correlation measurement of the data set shown in Figure 2c,d. A constant source-drain bias of 2 nA was applied to the functionalized (7, 5) SWCNT device at 77 K. (b) Representative scanning electron microscopy image of a SWCNT device where a single carbon nanotube was wired to a monolayer CVD graphene electrode pair. The scale bar equals 150 nm. (c) Collected photon count rates over the time period (∼38 ks) of intensity correlation measurement under 2 nA source-drain bias as in results shown in Figure 2c,d. The average count rate is 5.19 ± 2.97 kcps. (d) Accumulated histogram of the acquired photon count rates plotted with a bin size of 400 cps.

coincidence histograms in Figure 2, results are given in Figures S7 and S8. The simultaneously recorded photon count rate is plotted in Figure 4c and binned to a histogram in Figure 4d. The electrical power was maintained at a rather stable level despite an electrical noise of around 0.5 V (standard deviation of the recorded source-drain bias), as demonstrated in Figure S10a. The overlaid normal distribution curve of its histogram in Figure S10b indicates that the noise likely corresponds to Gaussian noise. The sudden changes of voltage in the time trace of the recorded bias may seem to refer to burst noise, however, this type of noise often has a time scale ranging from milliseconds to seconds. On the other hand, the large fluctuation of the count rate is attributed not only to the emitter properties itself but also to the setup stability. Due to the long measuring period, the sample mounted under the microscope would slowly drift away from the optimum focus point, mostly in the lateral position in the micrometer range, which caused a gradual decrease in the collected count rate over time and required moderate realignment in between data acquisition. Surprisingly, no correlation between the time trace of the dissipated electrical power and the count rate was found at the given time resolution (in seconds). Information on the mean values and the standard deviation are included in the figures.

To improve the data quality of the second-order correlation measurement of electrically driven single-photon emission and especially to shorten the long acquisition time, a few improved approaches may be attempted in the future. One would be to focus on boosting the light-collecting efficiency and/or the emission brightness without worrying too much about spectral purity and emission stability. For instance, in the recent work of Ovvyan et al.,[56] we showed that integrating the SWCNT device into photonic crystal cavities, in which 3D couplers were printed at the end of the nanowaveguides for read-out, not only increases the radiative emission rate but also reduces the collection loss in a free-space microscopic system. In our previous work, we estimated around 20% of emitted photon collection for 1400−1600 nm emission wavelength in free space with an objective (NA = 0.6).[48] On the other hand, the coupling efficiency of waveguide-integrated light emission[17,23] was reported around 60% and even above 98% for on-resonance coupling efficiency.[56] An additional advantage of integrating into cavities is that they also act as built-in filters of the photonic device for spectral cleaning.[57] Although according to the Purcell effect[58] the

emission rate enhancement (accelerated decay rate) in the cavity would indicate lifetime reduction as well, in principle, it should not be an issue providing the usage of low-jitter superconducting single-photon detectors.

Another approach is to improve the emission stability. Since the electroluminescence mainly originates from radiative carrier recombination of excitons, operating the device under stable conditions for exciton formation would be critical. However, hysteresis is, for example, one of the notorious issues for the device stability of low-dimensional carbon-based transistors. It is often related to the presence of charge trap states on the substrate or water molecules. A demonstration was represented in Figure S9 where 30 nm polytetrafluoroethylene (PTFE) was coated on the SWCNT device via liquid-phase deposition;[59] see the Methods Section. The electroluminescence spectrum and the intensity correlation histogram at 77 K are shown together with other results. Although still far from ideal, some improvements could be noticed, such as reduced electrical noise. A comparison between the electrical noise time trace of SWCNT devices with or without a PTFE layer is given in Figure S10. Another goal of passivation was to operate the device electrically at room temperature. Room-temperature transconductance curves and electroluminescence spectra are shown in Figure S11. With PTFE coating, clear suppression of hysteresis in the transconductance curves could be observed. Room-temperature electroluminescence with narrow emission lines was also achievable. The emission intensity and stability were, however, still not comparable to measurements at cryogenic temperature. Additional substrate treatment to decouple SWCNT/surface interaction may be necessary to further enhance the device/emission stability.[60]

CONCLUSION

In summary, single-photon emission from aryl-functionalized (7, 5) carbon nanotubes with sp^3 quantum defects triggered via electrical means at 77 K was demonstrated. We observed antibunching behavior by coupling excitonic or trionic defect-state electroluminescence into the fiber-coupled Hanbury–Brown–Twiss experiment setup. We further discussed the correlation between the zero-time delay second-order correlation function and the applied electrical power, including results regarding nonclassical emission of pristine carbon nanotubes below 4 K from previous work. Subsequently, we showed the relation between the full-width at half-maximum of the antibunching dips and the electrical power or emission wavelength. Challenges of performing electrically driven second-order correlation function measurements, for instance, maintaining bright/stable emission and improving photon collection efficiency, were also pointed out. Finally, suggestions and preliminary demonstrations are given which indicate how progress toward room-temperature single-photon electroluminescent emission can proceed.

METHODS SECTION

Dispersion and Functionalization of SWCNTs. The (7, 5) single-walled carbon nanotube dispersion was prepared by the procedure reported in our previous work.[37] In detail, 100 mg of the raw material soot (CoMoCAt, Sigma-Aldrich) and 100 mg of the polymer poly(9,9-di-*n*-octylfluorenyl-2,7-diyl) (PFO, Sigma-Aldrich) were dissolved in 100 mL of toluene. The suspension then went through a sonication treatment for 2 h using a titanium sonotrode (Bandelin, ∼20% power) while the suspension was placed in a water-circulation bath to aid cooling. After sonication, the suspension was centrifuged for 2 h at 20000*g*. To generate the starting suspensions for size-exclusion separation, the supernatant was concentrated to ∼10 mL by evaporating ∼90 mL of toluene. Semipreparative size exclusion chromatography was performed using Toyopearl HW-75 resin (Tosoh Bioscience) filled into a glass column having a 16 mm inner diameter and 20 cm length. For length sorting, 10 mL of starting suspension was loaded onto the column and flowed through the gel under gravity, at a flow rate of ∼2 mL/min, with toluene used as the eluent. Fractions with different length distributions were collected in 3–4 mL portions. For the functionalization, 100 μg of 3,5-dichlorophenyldiazonium tetrafluoroborate was added to 1 mL of a fraction with a suitable tube length (∼500 nm for this work) and heated on a heated plate, just below the boiling point of toluene, for 1 h. Right after the functionalization process, PL spectra were measured by using a home-built setup as described elsewhere.[61] UV–vis–NIR absorption spectra were recorded on a Varian Cary 500 spectrophotometer. Photoluminescence excitation maps were measured in the emission range of ∼900–1700 nm and excitation range of 500–950 nm (scanned in 3 nm steps) using a modified Fourier-transform infrared (FTIR) spectrometer (Bruker IFS66) equipped with a liquid nitrogen-cooled Ge-photodiode and a monochromatized excitation light source with a 250 W halogen lamp. The PL intensity was corrected for the wavelength-dependent excitation intensity and the instrumental response of the spectrometer.

Device Fabrication and SWCNT Deposition. The devices with graphene electrodes were fabricated from monolayer graphene on 300 nm thermal SiO_2 on p-type (B-doped) Si (Graphenea). Three electron-beam lithography steps (Leo 1530, Raith ElphyPlus) with proximity correction were required for patterning the electrodes. A schematic process flow of the device fabrication is shown in Figure S2. Poly(methyl methacrylate) (PMMA 950 K in Anisol) was used as a positive resist. Samples were spin-casted with resist and prebaked on a hot plate for 3 min at 150 °C. After the e-beam patterning, cold development was followed in a solution of methyl isobutyl ketone (MIBK) and isopropanol (1:3) for 30 s. Samples were rinsed with isopropanol, dried in a stream of nitrogen, and annealed at 90 °C for 1 min on a hot plate. In the first step of e-beam lithography, markers were defined, deposited with 50 nm tungsten by a sputtering technique (Bestec), and lifted off in acetone. In the second step, graphene strips were defined, and the remaining graphene apart from the PMMA-covered strips was etched via oxygen plasma (RIE Oxford Plasmalab 80 plus, 15 sccm O_2, 60 mTorr, 30 W for 75 s). The graphene strips had channel lengths of 150–200 nm and were perforated with holes to minimize the contact resistance. The bowtie-structured graphene strip used for setup alignment was also patterned in this step. Metal leads were defined in the last e-beam lithography step and subsequently deposited with 3 nm of chromium and 42 nm of palladium by sputtering. The lift-off process was carried out in acetone to complete the fabrication. The p-doped silicon substrate was used as a global back-gate electrode in all devices. Single chirality SWCNTs were integrated into the device using electric field-assisted dielectrophoresis.[47] The toluene-based suspension which has been used for photoluminescence excitation map measurement in Figure 1 was further diluted by a factor of 10–20 to obtain individual SWCNTs. Fifteen μL of suspension was drop-cast onto the device array, and DC bias between 0.1 and 2 V was applied on the common drain and the back-gate electrodes by using an Agilent 33250 function generator for 3 min. The samples were rinsed with toluene several times to remove excess polymer residue and dried with a nitrogen stream. The devices were annealed at 70 °C for 15 min to improve contact resistance before performing preliminary transport measurements. To confirm the successful deposition of SWCNT(s) between source-drain electrode pairs, transfer characteristics of the device were conducted at ambient conditions with a probe station using an Agilent 4155C semiconductor parameter analyzer. For biasing, we used separate source-measurement units (SMU) for each terminal: source, drain, and gate. The bias applied to the source and gate electrode was referenced to the drain potential. For devices coated with polytetrafluoroethylene (PTFE), a solution of poly(4,5-difluoro-2,2-bis(trifluoromethyl)-1,3-dioxole-*co*-tetrafluoroethylene) (Teflon AF-2400, Sigma-Aldrich) dissolved in Fluorinert FC-40 (Sigma-Aldrich) was prepared by stirring the solution for 2 weeks at 60 °C as presented

in the work of Kumar et al.[59] The solution was purified by removing the residual PTFE particles by ultracentrifugation for 1 h at 40000 rpm. A 30 nm PTFE layer deposition was achieved by spin-casting 1% purified PTFE solution (15 μL) at 3000 rpm for 60 s, followed by 100 °C for 5 min postannealing and subsequently ramped to 150 °C for another 5 min on the hot plate. All above-mentioned procedures were carried out in ambient conditions. To probe the metallic contact pads, direct electron beam patterning using an exposure dose of 2.6 mC/cm^2 at 10 keV beam energy was performed to remove PTFE.[62]

Optical Cryostat and Electroluminescence Spectroscopy Setup. The SWCNT devices were mounted on a home-built holder and loaded into a 4−500 K continuous-flow, sample-in-vacuum optical cryostat (MicrostatHiResII, Oxford Instruments). On-chip devices were electrically wire-bonded to the palladium pads on the sample holder. The samples were vacuum annealed (below 10^{-6} mbar) in situ at 70−120 °C via the integrated heater (ITC 503), and electroluminescence or correlation measurements were followed without breaking the vacuum. SWCNT devices were driven by using an Agilent 4155B semiconductor parameter analyzer where source-drain electrodes were operated in constant-current mode, whereas the gate electrode was running in constant-voltage mode. The 77 K cryogenic temperature was reached by introducing liquid nitrogen. The optical cryostat was positioned under a customized optical microscope (Zeiss Axiotech Vario) where the light from the emitter was collected with an objective (Olympus, LCPLN20XIR, 20×/NA = 0.45). The light was focused by a silver-coated off-axis parabolic mirror (MPD149-P01, f/4, Thorlabs) into an imaging spectrograph (Acton SP-2360, f/3.9, Princeton Instruments) and dispersed via diffraction grating (85 g/mm, 1.35 μm) onto a liquid-nitrogen-cooled 1024 × 1 pixels linear InGaAs photodiode array (PyLon-IR, Princeton Instruments) that was sensitive from 950 to 1610 nm. Wavelength calibration of the 1D InGaAs detector was performed by using the built-in function with a mercury−argon calibration light source (WITec). To compensate for the wavelength-dependent intensity scaling factor of the setup, the spectral sensitivity curve was acquired. The calibration of the spectral sensitivity and some more detail of the setup were described in our previous report.[48] The precise and stable positioning of the emitter was achieved via a motorized *xy* positioning stage (8MTF, Standa) along with a high-precision objective piezo scanner (P-721 PIFOC, Physik Instrumente) for tuning the focusing distance.

Correlation Measurement and Analysis of Functionalized SWCNTs at 77 K. To perform second-order correlation function, $g^2(\tau)$, measurements based on the Hanbury Brown and Twiss configuration, the SWCNT device was driven in a similar way to electroluminescence spectroscopy measurement in the optical cryostat at 77 K. The collected emission light was coupled into a single-mode 50/50 fused fiber coupler (TW1300R5F1 or TW1550R5F1, Thorlabs) via a protected silver reflective collimator (RC08APC-P01, Thorlabs) placed behind the objective with a spectral filter (Hard-Coated Bandpass/Longpass Filters, Thorlabs) mounted in between when required. The light was further guided to two separate fiber-coupled superconducting single-photon detectors (TCOPRS-CCR-TW35, SCONTEL) which are connected to the input channels of the time-correlated single-photon counting (PicoHarp 300, PicoQuant). The two low-jitter (≤35 ps) SSPDs were maintained at 2 K, well below the critical temperature, and at a constant DC bias around 90% of the critical current, such that a good compromise between high detection efficiency and low dark count rate, less than 100 cps, was achieved. The electrical signals generated from the SSPDs are sent to low-noise, high-frequency amplifiers (ZFL-1000LN+, Mini-Circuits) in negative polarity before reaching the input ports of the arrival time analyzer. The maximal measured count rate was on the order of 10 MHz limited by the dead time of a PicoHarp 300 instrument (∼90 ns). The SWCNT device was operated to emit light with a count rate of higher than 10^3 over 6−22 h to accumulate sufficient event pairs, and the analyzer recorded a $g^2(\tau)$ histogram by QuCoa software from PicoQuant in histogram or T2 mode with 8 or 12 ps bin sizes. To fit the experimental second-order correlation function measurement results, we normalized the collected coincidence histogram to the median value given the time delay axis shown in the figures. The median value instead of the mean value was used for normalization due to the low signal-to-noise ratio of the recorded histograms, and the median is less affected by the presence of outliers with extreme values. The data were fitted according to the correlation function, describing a sum of two exponential decays, $g^2(\tau) = 1 - c_1 e^{-\gamma_1|\tau-\tau_0|} - c_2 e^{-\gamma_2|\tau-\tau_0|}$ convoluted with the Gaussian distribution of time errors, $G(\tau) = 1/\sqrt{2\pi\sigma^2}\, e^{-\tau^2/2\sigma^2}$, where σ = 30 ps is the standard deviation of the jitter. From the convoluted function, a nonlinear least-squares fit based on the Levenberg−Marquardt algorithm was performed in which the fit results included the error estimation in terms of standard deviations, as described in detail in our previous work. Five parameters were extracted from the fit results, namely, the bunching/antibunching coefficient (c_1, c_2), the emission lifetime ($1/\gamma_1$, $1/\gamma_2$), and the zero-time delay (τ_0). The $g^2(0)$ values at the center of the antibunching dip were calculated based on these extracted parameters. At first, histograms composed of one direction of start−stop events in a given time window were fitted to determine the zero-time delay with the initial guess for the fit parameters of $c_1 = -0.1$, $c_2 = 0.8$, $\gamma_1 = 0.5$ GHz, $\gamma_2 = 5$ GHz, and $\tau_0 = 0.4$ ns. The extracted τ_0 values were then used to compensate for the time offset to comprise histograms of bidirectional start−stop pairs, as demonstrated in Figure S5. To extract more precise $g^2(0)$ values, we selected the antibunching dip region for fitting as the data quality was not optimum with the initial guess for the fit parameters of $c_1 = 0$ (fixed), $c_2 = 0.8$, $\gamma_2 = 5$ GHz, and $\tau_0 = 0$. In the nonlinear procedure, the iterations were repeated until the fitting parameters stabilized up to the ninth significant digit. As a side note, the two different fitting conditions show little effect on the extracted value of τ_0 but better fitting results at the center of the antibunching dips. For the photon bunching measurement to determine the system time delay, we replaced the SWCNT device with a 1550 nm laser diode (LPS-1550-FC, Thorlabs). We directly coupled emission light into the two SSPDs via a 50/50 1550 nm fused fiber coupler (TW1550R5F1, Thorlabs) without a reflective collimator. The laser intensity was greatly attenuated to avoid count rate overflow, and an in-line fiber polarizer (ILP1550SM-FC, Thorlabs) was attached before photon splitting. The remaining data acquisition was similar to that for an SWCNT intensity correlation measurement. Results are shown in the Supporting Information.

AUTHOR INFORMATION

Corresponding Authors

Min-Ken Li − *Institute of Quantum Materials and Technologies, Karlsruhe Institute of Technology, 76131 Karlsruhe, Germany; Institute of Materials Science, Technische Universität Darmstadt, 64287 Darmstadt, Germany;* orcid.org/0000-0002-6012-4721; Email: min-ken.li@kit.edu

Ralph Krupke − *Institute of Quantum Materials and Technologies, Karlsruhe Institute of Technology, 76131 Karlsruhe, Germany; Institute of Materials Science, Technische Universität Darmstadt, 64287 Darmstadt, Germany; Institute of Nanotechnology, Karlsruhe Institute of Technology, 76131 Karlsruhe, Germany;* orcid.org/0000-0001-8427-8592; Email: ralph.krupke@kit.edu

Authors

Simone Dehm − *Institute of Nanotechnology, Karlsruhe Institute of Technology, 76131 Karlsruhe, Germany*

Manfred M. Kappes − *Institute of Quantum Materials and Technologies, Karlsruhe Institute of Technology, 76131 Karlsruhe, Germany; Institute of Nanotechnology and Institute of Physical Chemistry, Karlsruhe Institute of Technology, 76131 Karlsruhe, Germany;* orcid.org/0000-0002-1199-1730

Frank Hennrich − *Institute of Quantum Materials and Technologies, Karlsruhe Institute of Technology, 76131 Karlsruhe, Germany*

Author Contributions

The experiments were conceived and designed by R.K., M.L., and F.H. Dispersions with functionalized (7, 5) SWCNTs were prepared by F.H . Devices were fabricated and subjected to charge-transport, electroluminescence, and intensity correlation measurements by M.L. and S.D. Photoluminescence measurements were performed by F.H. The manuscript was written by M.L. and R.K. with input from all coauthors.

Notes

The authors declare no competing financial interest.

ACKNOWLEDGMENTS

M.L., S.D., F.H., M.K., and R.K. acknowledge support from the Helmholtz Research Programs Natural, Artificial, and Cognitive Information Processing (NACIP), and by the Karlsruhe Nano Micro Facility (KNMF).

REFERENCES

(1) O'Mahony, M. J.; Politi, C.; Klonidis, D.; Nejabati, R.; Simeonidou, D. Future Optical Networks. *Journal of Lightwave Technology* **2006**, *24* (12), 4684−4696.

(2) Shacham, A.; Bergman, K.; Carloni, L. P. Photonic Networks-on-Chip for Future Generations of Chip Multiprocessors. *IEEE Transactions on Computers* **2008**, *57* (9), 1246−1260.

(3) Knill, E.; Laflamme, R.; Milburn, G. J. A Scheme for Efficient Quantum Computation with Linear Optics. *Nature* **2001**, *409* (6816), 46−52.

(4) O'Brien, J. L. Optical Quantum Computing. *Science* **2007**, *318* (5856), 1567−1570.

(5) O'Brien, J. L.; Furusawa, A.; Vučković, J. Photonic Quantum Technologies. *Nat. Photonics* **2009**, *3* (12), 687−695.

(6) Deshpande, S.; Heo, J.; Das, A.; Bhattacharya, P. Electrically Driven Polarized Single-Photon Emission from an InGaN Quantum Dot in a GaN Nanowire. *Nat. Commun.* **2013**, *4* (1), 1675.

(7) Heindel, T.; Schneider, C.; Lermer, M.; Kwon, S. H.; Braun, T.; Reitzenstein, S.; Höfling, S.; Kamp, M.; Forchel, A. Electrically Driven Quantum Dot-Micropillar Single Photon Source with 34% Overall Efficiency. *Appl. Phys. Lett.* **2010**, *96* (1), 011107.

(8) Lohrmann, A.; Pezzagna, S.; Dobrinets, I.; Spinicelli, P.; Jacques, V.; Roch, J.-F.; Meijer, J.; Zaitsev, A. M. Diamond Based Light-Emitting Diode for Visible Single-Photon Emission at Room Temperature. *Appl. Phys. Lett.* **2011**, *99* (25), 251106.

(9) Mizuochi, N.; Makino, T.; Kato, H.; Takeuchi, D.; Ogura, M.; Okushi, H.; Nothaft, M.; Neumann, P.; Gali, A.; Jelezko, F.; Wrachtrup, J.; Yamasaki, S. Electrically Driven Single-Photon Source at Room Temperature in Diamond. *Nat. Photonics* **2012**, *6* (5), 299−303.

(10) Palacios-Berraquero, C.; Barbone, M.; Kara, D. M.; Chen, X.; Goykhman, I.; Yoon, D.; Ott, A. K.; Beitner, J.; Watanabe, K.; Taniguchi, T.; Ferrari, A. C.; Atatüre, M. Atomically Thin Quantum Light-Emitting Diodes. *Nat. Commun.* **2016**, *7* (1), 12978.

(11) Chakraborty, C.; Kinnischtzke, L.; Goodfellow, K. M.; Beams, R.; Vamivakas, A. N. Voltage-Controlled Quantum Light from an Atomically Thin Semiconductor. *Nat. Nanotechnol* **2015**, *10* (6), 507−511.

(12) He, X.; Htoon, H.; Doorn, S. K.; Pernice, W. H. P.; Pyatkov, F.; Krupke, R.; Jeantet, A.; Chassagneux, Y.; Voisin, C. Carbon Nanotubes as Emerging Quantum-Light Sources. *Nat. Mater.* **2018**, *17* (8), 663−670.

(13) Avouris, P.; Freitag, M.; Perebeinos, V. Carbon-Nanotube Photonics and Optoelectronics. *Nat. Photonics* **2008**, *2* (6), 341−350.

(14) Bachilo, S. M.; Strano, M. S.; Kittrell, C.; Hauge, R. H.; Smalley, R. E.; Weisman, R. B. Structure-Assigned Optical Spectra of Single-Walled Carbon Nanotubes. *Science* **2002**, *298* (5602), 2361−2366.

(15) Freitag, M.; Perebeinos, V.; Chen, J.; Stein, A.; Tsang, J. C.; Misewich, J. A.; Martel, R.; Avouris, P. Hot Carrier Electroluminescence from a Single Carbon Nanotube. *Nano Lett.* **2004**, *4* (6), 1063−1066.

(16) Chen, J.; Perebeinos, V.; Freitag, M.; Tsang, J.; Fu, Q.; Liu, J.; Avouris, P. Bright Infrared Emission from Electrically Induced Excitons in Carbon Nanotubes. *Science* **2005**, *310* (5751), 1171−1174.

(17) Khasminskaya, S.; Pyatkov, F.; Flavel, B. S.; Pernice, W. H.; Krupke, R. Waveguide-Integrated Light-Emitting Carbon Nanotubes. *Adv. Mater.* **2014**, *26* (21), 3465−3472.

(18) Jeantet, A.; Chassagneux, Y.; Claude, T.; Roussignol, P.; Lauret, J. S.; Reichel, J.; Voisin, C. Exploiting One-Dimensional Exciton-Phonon Coupling for Tunable and Efficient Single-Photon Generation with a Carbon Nanotube. *Nano Lett.* **2017**, *17* (7), 4184−4188.

(19) Vijayaraghavan, A.; Blatt, S.; Weissenberger, D.; Oron-Carl, M.; Hennrich, F.; Gerthsen, D.; Hahn, H.; Krupke, R. Ultra-Large-Scale Directed Assembly of Single-Walled Carbon Nanotube Devices. *Nano Lett.* **2007**, *7* (6), 1556−1560.

(20) Ganzhorn, M.; Vijayaraghavan, A.; Green, A. A.; Dehm, S.; Voigt, A.; Rapp, M.; Hersam, M. C.; Krupke, R. A Scalable, CMOS-Compatible Assembly of Ambipolar Semiconducting Single-Walled Carbon Nanotube Devices. *Adv. Mater.* **2011**, *23* (15), 1734−1738.

(21) Hills, G.; Lau, C.; Wright, A.; Fuller, S.; Bishop, M. D.; Srimani, T.; Kanhaiya, P.; Ho, R.; Amer, A.; Stein, Y.; Murphy, D.; Arvind; Chandrakasan, A.; Shulaker, M. M. Modern Microprocessor Built from Complementary Carbon Nanotube Transistors. *Nature* **2019**, *572* (7771), 595−602.

(22) Hofmann, M. S.; Glückert, J. T.; Noé, J.; Bourjau, C.; Dehmel, R.; Högele, A. Bright, Long-Lived and Coherent Excitons in Carbon Nanotube Quantum Dots. *Nat. Nanotechnol* **2013**, *8* (7), 502−505.

(23) Khasminskaya, S.; Pyatkov, F.; Słowik, K.; Ferrari, S.; Kahl, O.; Kovalyuk, V.; Rath, P.; Vetter, A.; Hennrich, F.; Kappes, M. M.; Gol'tsman, G.; Korneev, A.; Rockstuhl, C.; Krupke, R.; Pernice, W. H. P. Fully Integrated Quantum Photonic Circuit with an Electrically Driven Light Source. *Nat. Photonics* **2016**, *10* (11), 727−732.

(24) Ma, X.; Adamska, L.; Yamaguchi, H.; Yalcin, S. E.; Tretiak, S.; Doorn, S. K.; Htoon, H. Electronic Structure and Chemical Nature of Oxygen Dopant States in Carbon Nanotubes. *ACS Nano* **2014**, *8* (10), 10782−10789.

(25) Ghosh, S.; Bachilo, S. M.; Simonette, R. A.; Beckingham, K. M.; Weisman, R. B. Oxygen Doping Modifies Near-Infrared Band Gaps in Fluorescent Single-Walled Carbon Nanotubes. *Science* **2010**, *330* (6011), 1656−1659.

(26) Janas, D. Perfectly Imperfect: A Review of Chemical Tools for Exciton Engineering in Single-Walled Carbon Nanotubes. *Mater. Horiz* **2020**, *7* (11), 2860−2881.

(27) Kwon, H.; Furmanchuk, A.; Kim, M.; Meany, B.; Guo, Y.; Schatz, G. C.; Wang, Y. Molecularly Tunable Fluorescent Quantum Defects. *J. Am. Chem. Soc.* **2016**, *138* (21), 6878−6885.

(28) Shiraki, T.; Miyauchi, Y.; Matsuda, K.; Nakashima, N. Carbon Nanotube Photoluminescence Modulation by Local Chemical and Supramolecular Chemical Functionalization. *Acc. Chem. Res.* **2020**, *53* (9), 1846−1859.

(29) Hartmann, N. F.; Velizhanin, K. A.; Haroz, E. H.; Kim, M.; Ma, X.; Wang, Y.; Htoon, H.; Doorn, S. K. Photoluminescence Dynamics of

Aryl Sp ^{3} Defect States in Single-Walled Carbon Nanotubes. *ACS Nano* **2016**, *10* (9), 8355−8365.
(30) He, X.; Velizhanin, K. A.; Bullard, G.; Bai, Y.; Olivier, J.-H.; Hartmann, N. F.; Gifford, B. J.; Kilina, S.; Tretiak, S.; Htoon, H.; Therien, M. J.; Doorn, S. K. Solvent- and Wavelength-Dependent Photoluminescence Relaxation Dynamics of Carbon Nanotube Sp ^{3} Defect States. *ACS Nano* **2018**, *12* (8), 8060−8070.
(31) Piao, Y.; Meany, B.; Powell, L. R.; Valley, N.; Kwon, H.; Schatz, G. C.; Wang, Y. Brightening of Carbon Nanotube Photoluminescence through the Incorporation of Sp3 Defects. *Nat. Chem.* **2013**, *5* (10), 840−845.
(32) Ma, X.; Hartmann, N. F.; Baldwin, J. K. S.; Doorn, S. K.; Htoon, H. Room-Temperature Single-Photon Generation from Solitary Dopants of Carbon Nanotubes. *Nat. Nanotechnol* **2015**, *10* (8), 671−675.
(33) He, X.; Hartmann, N. F.; Ma, X.; Kim, Y.; Ihly, R.; Blackburn, J. L.; Gao, W.; Kono, J.; Yomogida, Y.; Hirano, A.; Tanaka, T.; Kataura, H.; Htoon, H.; Doorn, S. K. Tunable Room-Temperature Single-Photon Emission at Telecom Wavelengths from Sp3 Defects in Carbon Nanotubes. *Nat. Photonics* **2017**, *11* (9), 577−582.
(34) Zorn, N. F.; Berger, F. J.; Zaumseil, J. Charge Transport in and Electroluminescence from Sp ^{3} -Functionalized Carbon Nanotube Networks. *ACS Nano* **2021**, *15* (6), 10451−10463.
(35) Xu, B.; Wu, X.; Kim, M.; Wang, P.; Wang, Y. Electroluminescence from 4-Nitroaryl Organic Color Centers in Semiconducting Single-Wall Carbon Nanotubes. *J. Appl. Phys.* **2021**, *129* (4), 044305.
(36) Li, M.-K.; Riaz, A.; Wederhake, M.; Fink, K.; Saha, A.; Dehm, S.; He, X.; Schöppler, F.; Kappes, M. M.; Htoon, H.; Popov, V. N.; Doorn, S. K.; Hertel, T.; Hennrich, F.; Krupke, R. Electroluminescence from Single-Walled Carbon Nanotubes with Quantum Defects. *ACS Nano* **2022**, *16* (8), 11742−11754.
(37) Hennrich, F.; Li, W.; Fischer, R.; Lebedkin, S.; Krupke, R.; Kappes, M. M. Length-Sorted, Large-Diameter, Polyfluorene-Wrapped Semiconducting Single-Walled Carbon Nanotubes for High-Density, Short-Channel Transistors. *ACS Nano* **2016**, *10* (2), 1888−1895.
(38) Kadria-Vili, Y.; Bachilo, S. M.; Blackburn, J. L.; Weisman, R. B. Photoluminescence Side Band Spectroscopy of Individual Single-Walled Carbon Nanotubes. *J. Phys. Chem. C* **2016**, *120* (41), 23898−23904.
(39) Cambré, S.; Santos, S. M.; Wenseleers, W.; Nugraha, A. R. T.; Saito, R.; Cognet, L.; Lounis, B. Luminescence Properties of Individual Empty and Water-Filled Single-Walled Carbon Nanotubes. *ACS Nano* **2012**, *6* (3), 2649−2655.
(40) Hartmann, N. F.; Pramanik, R.; Dowgiallo, A.-M.; Ihly, R.; Blackburn, J. L.; Doorn, S. K. Photoluminescence Imaging of Polyfluorene Surface Structures on Semiconducting Carbon Nanotubes: Implications for Thin Film Exciton Transport. *ACS Nano* **2016**, *10* (12), 11449−11458.
(41) Blackburn, J. L.; Holt, J. M.; Irurzun, V. M.; Resasco, D. E.; Rumbles, G. Confirmation of K-Momentum Dark Exciton Vibronic Sidebands Using ^{13} C-Labeled, Highly Enriched (6,5) Single-Walled Carbon Nanotubes. *Nano Lett.* **2012**, *12* (3), 1398−1403.
(42) Miyauchi, Y.; Iwamura, M.; Mouri, S.; Kawazoe, T.; Ohtsu, M.; Matsuda, K. Brightening of Excitons in Carbon Nanotubes on Dimensionality Modification. *Nat. Photonics* **2013**, *7* (9), 715−719.
(43) Qu, H.; Wu, X.; Fortner, J.; Kim, M.; Wang, P.; Wang, Y. Reconfiguring Organic Color Centers on the Sp ^{2} Carbon Lattice of Single-Walled Carbon Nanotubes. *ACS Nano* **2022**, *16* (2), 2077−2087.
(44) He, X.; Gifford, B. J.; Hartmann, N. F.; Ihly, R.; Ma, X.; Kilina, S. V.; Luo, Y.; Shayan, K.; Strauf, S.; Blackburn, J. L.; Tretiak, S.; Doorn, S. K.; Htoon, H. Low-Temperature Single Carbon Nanotube Spectroscopy of Sp ^{3} Quantum Defects. *ACS Nano* **2017**, *11* (11), 10785−10796.
(45) Saha, A.; Gifford, B. J.; He, X.; Ao, G.; Zheng, M.; Kataura, H.; Htoon, H.; Kilina, S.; Tretiak, S.; Doorn, S. K. Narrow-Band Single-Photon Emission through Selective Aryl Functionalization of Zigzag Carbon Nanotubes. *Nat. Chem.* **2018**, *10* (11), 1089−1095.
(46) Settele, S.; Berger, F. J.; Lindenthal, S.; Zhao, S.; El Yumin, A. A.; Zorn, N. F.; Asyuda, A.; Zharnikov, M.; Högele, A.; Zaumseil, J. Synthetic Control over the Binding Configuration of Luminescent Sp3-Defects in Single-Walled Carbon Nanotubes. *Nat. Commun.* **2021**, *12* (1), 2119.
(47) Li, W.; Hennrich, F.; Flavel, B. S.; Dehm, S.; Kappes, M.; Krupke, R. Principles of Carbon Nanotube Dielectrophoresis. *Nano Res.* **2021**, *14* (7), 2188−2206.
(48) Gaulke, M.; Janissek, A.; Peyyety, N. A.; Alamgir, I.; Riaz, A.; Dehm, S.; Li, H.; Lemmer, U.; Flavel, B. S.; Kappes, M. M.; Hennrich, F.; Wei, L.; Chen, Y.; Pyatkov, F.; Krupke, R. Low-Temperature Electroluminescence Excitation Mapping of Excitons and Trions in Short-Channel Monochiral Carbon Nanotube Devices. *ACS Nano* **2020**, *14* (3), 2709−2717.
(49) Engel, M.; Steiner, M.; Lombardo, A.; Ferrari, A. C.; Löhneysen, H. v.; Avouris, P.; Krupke, R. Light-Matter Interaction in a Microcavity-Controlled Graphene Transistor. *Nat. Commun.* **2012**, *3* (1), 906.
(50) Nutz, M.; Zhang, J.; Kim, M.; Kwon, H.; Wu, X.; Wang, Y.; Högele, A. Photon Correlation Spectroscopy of Luminescent Quantum Defects in Carbon Nanotubes. *Nano Lett.* **2019**, *19* (10), 7078−7084.
(51) Kwon, H.; Kim, M.; Nutz, M.; Hartmann, N. F.; Perrin, V.; Meany, B.; Hofmann, M. S.; Clark, C. W.; Htoon, H.; Doorn, S. K.; Högele, A.; Wang, Y. Probing Trions at Chemically Tailored Trapping Defects. *ACS Cent Sci.* **2019**, *5* (11), 1786−1794.
(52) Högele, A.; Galland, C.; Winger, M.; Imamoğlu, A. Photon Antibunching in the Photoluminescence Spectra of a Single Carbon Nanotube. *Phys. Rev. Lett.* **2008**, *100* (21), 217401.
(53) Aharonovich, I.; Englund, D.; Toth, M. Solid-State Single-Photon Emitters. *Nat. Photonics* **2016**, *10* (10), 631−641.
(54) Tan, P. K.; Yeo, X. J.; Leow, A. Z. W.; Shen, L.; Kurtsiefer, C. Practical Range Sensing with Thermal Light. *Phys. Rev. Appl.* **2023**, *20* (1), 014060.
(55) Ogawa, K. Analysis of Mode Partition Noise in Laser Transmission Systems. *IEEE J. Quantum Electron.* **1982**, *18* (5), 849−855.
(56) Ovvyan, A. P.; Li, M.-K.; Gehring, H.; Beutel, F.; Kumar, S.; Hennrich, F.; Wei, L.; Chen, Y.; Pyatkov, F.; Krupke, R.; Pernice, W. H. P. An Electroluminescent and Tunable Cavity-Enhanced Carbon-Nanotube-Emitter in the Telecom Band. *Nat. Commun.* **2023**, *14* (1), 3933.
(57) Borel, A.; Habrant-Claude, T.; Rapisarda, F.; Reichel, J.; Doorn, S. K.; Voisin, C.; Chassagneux, Y. Telecom Band Single-Photon Source Using a Grafted Carbon Nanotube Coupled to a Fiber Fabry-Perot Cavity in the Purcell Regime. *ACS Photonics* **2023**, *10* (8), 2839−2845.
(58) Purcell, E. M.; Torrey, H. C.; Pound, R. V. Resonance Absorption by Nuclear Magnetic Moments in a Solid. *Phys. Rev.* **1946**, *69* (1−2), 37−38.
(59) Kumar, S.; Dagli, D.; Dehm, S.; Das, C.; Wei, L.; Chen, Y.; Hennrich, F.; Krupke, R. Vanishing Hysteresis in Carbon Nanotube Transistors Embedded in Boron Nitride/Polytetrafluoroethylene Heterolayers. *physica status solidi (RRL) - Rapid Research Letters* **2020**, *14* (8), 2000193.
(60) Zorn, N. F.; Settele, S.; Zhao, S.; Lindenthal, S.; El Yumin, A. A.; Wedl, T.; Li, H.; Flavel, B. S.; Högele, A.; Zaumseil, J. Near-Intrinsic Photo- and Electroluminescence from Single-Walled Carbon Nanotube Thin Films on BCB-Passivated Surfaces. *Adv. Opt Mater.* **2023**, *11* (14), 2300236.
(61) Lebedkin, S.; Hennrich, F.; Kiowski, O.; Kappes, M. M. Photophysics of Carbon Nanotubes in Organic Polymer-Toluene Dispersions: Emission and Excitation Satellites and Relaxation Pathways. *Phys. Rev. B* **2008**, *77* (16), 165429.
(62) Karre, V.; Keathley, P. D.; Guo, J.; Hastings, J. T. Direct Electron-Beam Patterning of Teflon AF. *IEEE Trans Nanotechnol* **2009**, *8* (2), 139−141.